applied sciences

MDPI

Article

Structural Improvement of Differential Motion Assembly in In Situ Pressure-Preserved Coring System Using CFD Simulation

Da Guo [1,2,3], Jianan Li [2,*], Dingming Wang [2,3], Yiwei Zhang [2,3], Xin Fang [2,3] and Heping Xie [2,3]

[1] School of Mechanical Engineering, Sichuan University, Chengdu 610065, China
[2] MOE Key Laboratory of Deep Underground Science and Engineering, College of Water Resource and Hydropower, Sichuan University, Chengdu 610065, China
[3] Guangdong Provincial Key Laboratory of Deep Earth Sciences and Geothermal Energy Exploitation and Utilization, Institute of Deep Earth Sciences and Green Energy, College of Civil and Transportation Engineering, Shenzhen University, Shenzhen 518060, China
* Correspondence: lijn2013@163.com

Abstract: In situ pressure-preserved coring (IPP-Coring) is one of the most efficient methods for identifying the scale of the oil and gas content. However, the differential motion assembly of the IPP-Coring system often undergoes ball and ball seat seal failure and sticking due to surface erosion, and a greater pressure drop may unexpectedly trigger the assembly. This paper addresses these issues by improving the hydraulic structure of an assembly based on a deep understanding of the flow characteristics in the assembly, thus increasing the success rate of the IPP-Coring. Computational fluid dynamics (CFD) was employed to investigate flows in a differential motion assembly. The effects of the diameter and outlet structure of the ball seat on the fluid status, velocity, and pressure distribution were thoroughly analyzed. When the ball seat diameter increased from 30 to 40 mm, the maximum velocity and pressure drop decreased to 0.55 and 0.2 times their original values, respectively. There was a severe vortex area in the differential motion assembly due to the presence of the ball seat, but changing the outlet structure in the ball seat to an arc structure decreased the length of the vortex area and the fluid velocity near the wall to 0.7 and 0.4 times, respectively, compared with those with the original right-angled structure. In addition, the pressure drop decreased to 0.33 times the original value. Thus, the hydraulic structure of the assembly was improved, and a 40 mm diameter ball seat and an arc-shaped ball seat outlet were selected. Particle trajectory and erosion calculation results showed that the improved structure has a lower particle velocity and less impact on the wall, and the average erosion rate is only 0.42 times the value of the original structure. Due to the better erosion resistance and smaller pressure drop, the improved structure shows promise for field performance.

Keywords: differential motion assembly; in situ coring; erosion; flow characteristics; computational fluid dynamics

check for updates

Citation: Guo, D.; Li, J.; Wang, D.; Zhang, Y.; Fang, X.; Xie, H. Structural Improvement of Differential Motion Assembly in In Situ Pressure-Preserved Coring System Using CFD Simulation. *Appl. Sci.* **2023**, *13*, 4108. https://doi.org/10.3390/app13074108

Academic Editor: Francesca Scargiali

Received: 25 February 2023
Revised: 18 March 2023
Accepted: 22 March 2023
Published: 23 March 2023

Copyright: © 2023 by the authors. Licensee MDPI, Basel, Switzerland. This article is an open access article distributed under the terms and conditions of the Creative Commons Attribution (CC BY) license (https://creativecommons.org/licenses/by/4.0/).

1. Introduction

With the exhaustion of resources at shallow depths in the earth, the development of resources is gradually occurring at greater depths [1–3]. At present, the depth of coal mining exceeds 1500 m, metal mining has reached 4350 m, and oil and gas resource mining has reached 7500 m [4–7]. The exploitation and utilization of deep resources require accurate knowledge of reservoir scale and properties. Coring is a vital method used in exploration; it can obtain core samples from subsurface formations. By analyzing core samples, reliable information about the rock and fluid properties can be obtained, and then the scale of the reservoir content can be identified [3,8]. However, for conventional coring technology, the change in pressure during tripping can expel fluid and gas components from the core sample, resulting in a large error between the reserve assessment values and the real situation of the deep resource [9–13]. Field tests conducted by Bjorum et al. have

shown that for conventional coring technology, more than 50% of the fluid and gas can be lost from a sample due to fluid expulsion during tripping [14].

To overcome this issue, in situ pressure-preserved coring (IPP-Coring) technology has been introduced for deep exploration [15–19]. This technology avoids fluid expulsion by maintaining the core pressure at the bottom hole pressure, thereby making it possible to accurately assess the scale of the reservoir contents [20–23]. At present, scholars around the world have performed much research on in situ pressure-preserved coring technology and developed many types of IPP-Coring equipment. For example, to obtain cores from offshore gas hydrates for research, the pressure core barrel (PCB), advanced piston corer (APC), pressure core sampler (PCS), hydrate autoclave coring equipment system (HY-ACE), and pressure temperature core sampler (PTCS) have been developed by different countries and institutions in the past few years [24–30]. For onshore coring for deep oil and gas exploration, the GWY194-70BB and GW-CP194-80A pressure coring systems are two typical types of IPP-Coring equipment; their pressure preservation capacities can reach 20 and 60 MPa, respectively [31,32]. In current IPP-Coring devices, their pressure preservation principle is mainly the closure of a ball valve or flap valve to form a sealed chamber to maintain the in situ pressure of the core sample. The closure of the valves depends on the relative movement between the core (inner) pipe and the outer pipe through a mechanical device such as an overshot assembly or a hydrodynamic-pressure lifting device such as a differential motion assembly. In onshore deep oil and gas exploration, due to the small inner diameters of common oil drill pipes, tripping the mechanical device in the hole has been a problem; usually, it is necessary to use specialized drill pipes, which wastes considerable effort and cost. Therefore, relative movement between the core tube and outer tube often depends on the hydrodynamic-pressure lifting device in onshore deep oil and gas explorations, namely, the differential motion assembly in this study [32].

The working principle of the differential motion assembly used to realize the pressure preservation operation of the IPP-Coring system for onshore oil and gas explorations is shown in Figure 1. In the coring operation, the upper section of the IPP-Coring system is successively connected to the drill collars and drill pipes in the bottom hole assembly. When coring begins, the drilling fluid passes through the inside of the differential motion assembly, and the valve cover in the valve assembly stays open due to the constraint of the inner pipe. At the end of drilling, the rock core enters the in situ pressure-preserved core chamber. At this time, a steel ball is dropped into the hole and dropped onto the ball seat, which changes the drilling fluid path from the interior to the outer part of the differential motion assembly, as shown by the red arrow. Under the action of hydrodynamic pressure, two limit pins are cut off, and the differential motion assembly is lifted to drive the inner pipe up over the valve cover. Then, the valve cover automatically closes under the action of gravity to maintain the in situ pressure. According to this working principle, the differential motion assembly plays a vital role in the process of IPP-Coring during onshore oil and gas exploration, and it directly determines the success rate of IPP-Coring. Unfortunately, in the field service process, due to the complex deep well environment characterized by high pressure and temperature, high flow rates, and solids content of the drilling fluid, the differential motion assembly is often faced with the failure of the seal of the ball and ball seat as well as sticking caused by surface erosion. In addition, in the case of large positive displacement pumps, the differential motion assembly may be lifted at the wrong time (the pin is cut off before the ball is dropped) due to the greater pressure drop, which contributes to the failure of IPP-Coring. Therefore, it is necessary to improve the hydraulic structure of the differential motion assembly to decrease the surface erosion and pressure drop to further increase its reliability and service life.

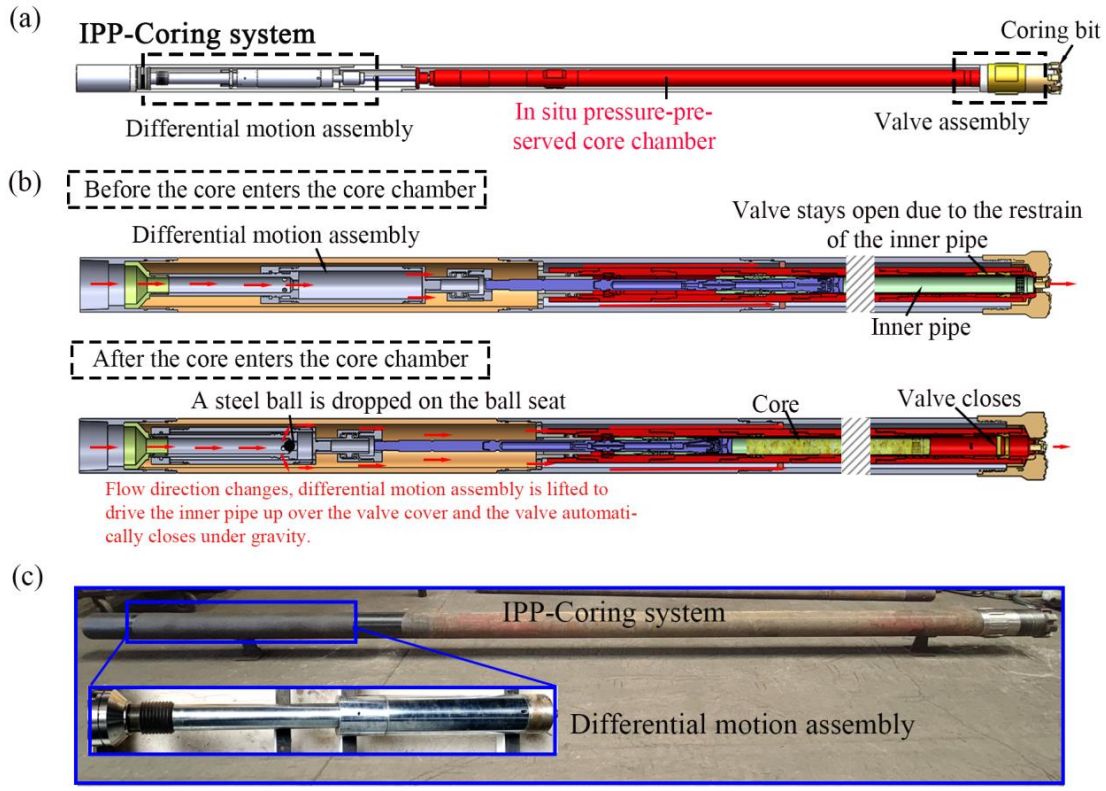


Figure 1. (**a**) Schematic diagram of the IPP-Coring system. (**b**) Schematic diagram of the working principle of the IPP-Coring system and the differential motion assembly. (**c**) Photographs of the IPP-Coring system and the differential motion assembly.

To improve the hydraulic structure, it is necessary to have a deep insight into the flow characteristics of the drilling fluid in the differential motion assembly. Computational fluid dynamics (CFD) can effectively analyze the flow characteristics of downhole tools [33–38]. However, there has been little research on flow characteristics in differential motion assemblies in the IPP-Coring systems used in deep oil and gas exploration. The effects of the internal size and structure of the differential motion assembly on the flow velocity and pressure distribution are unclear, and it is impossible to target the design of the hydraulic structure to reduce erosion and pressure drop. As a result, the operational reliability and service life of differential motion assemblies have been low, which would result in a low success rate of the IPP-Coring. To increase the operational reliability and service life of differential motion assemblies and increase the success rate of IPP-Coring, this study employed CFD with the standard k-ε turbulence model to study the characteristics of flows with different rates in a differential motion assembly during IPP-Coring. The effects of the diameter of the ball seat and ball seat outlet structure on the fluid status, velocity, and pressure distribution were analyzed. Further, the hydraulic structure of the differential motion assembly was improved, and field experiments demonstrated the erosion resistance of the improved structure.

2. Numerical Simulation

2.1. Mathematical Model

2.1.1. Liquid Phase Model

During running, the drilling fluid flows through the differential motion assembly. The continuity equations and momentum equations are as follows [39]:

$$\frac{\partial \rho}{\partial t} + \nabla \cdot \left(\rho \vec{u} \right) = 0 \tag{1}$$

$$\frac{\partial}{\partial t}\left(\rho\vec{u}\right)+\nabla\cdot\left(\rho\vec{u}\vec{u}\right)=-\nabla P+\nabla\cdot\left\{\mu\left[\left(\nabla\vec{u}+\nabla\vec{u}^{T}\right)-\frac{2}{3}\nabla\cdot\vec{u}I\right]\right\}+\rho\vec{g}+\vec{s}_{M} \quad (2)$$

where ρ is the liquid phase density, $\vec{u}$ represents the instantaneous velocity vector, P is pressure, μ is the molecular viscosity, I is the unit tensor, $\rho\vec{g}$ is the gravitational body force, and S_M is the added momentum caused by the discrete phase.

The standard k-ε model is very popular in industrial flow and heat transfer simulations because of its robustness and economy, and it has shown reasonable accuracy for fully developed turbulent flow conditions [40]. For the differential motion assembly, during the IPP-Coring process for deep oil and gas exploration, the drilling fluid, which is characterized by a high velocity (pump displacement can reach 20~40 L/s), high pressure, and high solid particle content, circulates through it. Due to the high velocity and the resulting high Reynolds number, the flow in the differential motion assembly is usually turbulent. Thus, the standard k-ε model, which has reasonable accuracy for a wide range of turbulent flows and a fast convergence rate [40], was employed in this study to gain an insight into the flow characteristics in the differential motion assembly. The equations are as follows [39,41,42]:

$$\frac{\partial(\rho k)}{\partial t}+\frac{\partial(\rho k u_i)}{\partial x_i}=\frac{\partial}{\partial x_j}\left[\left(\mu+\frac{\mu_T}{\sigma_k}\right)\frac{\partial k}{\partial x_j}\right]+P_k-\rho\varepsilon+S_k \quad (3)$$

$$\frac{\partial(\rho\varepsilon)}{\partial t}+\frac{\partial(\rho\varepsilon u_i)}{\partial x_i}=\frac{\partial}{\partial x_j}\left[\left(\mu+\frac{\mu_T}{\sigma_\varepsilon}\right)\frac{\partial\varepsilon}{\partial x_j}\right]+C_{\varepsilon1}\frac{\varepsilon}{k}P_k-C_{\varepsilon2}\rho\frac{\varepsilon^2}{k}+S_\varepsilon \quad (4)$$

$$P_k=\mu_T\nabla\vec{u}\cdot\left(\nabla\vec{u}+\nabla\vec{u}^{T}\right)-\frac{2}{3}\nabla\vec{u}\left(3\mu_T\nabla\cdot\vec{u}+\rho k\right) \quad (5)$$

$$\mu_T=\rho C_\mu\frac{k^2}{\varepsilon} \quad (6)$$

where μ_T is the turbulent eddy viscosity; k and ε are the turbulent kinetic energy and the turbulent dissipation rate, respectively; u_i denotes the velocity component in the i-direction; x_i and x_j are the coordinates in space; $C_{\varepsilon1}, C_{\varepsilon2}$, and C_μ are model constants; S_k and S_ε represent the source terms defined by the discrete phase caused by the particle damping and turbulence eddies; σ_k and σ_ε denote the turbulent Prandtl numbers; and P_k is the kinetic energy of the turbulence caused by the mean velocity gradients. In the standard k-ε model, $C_\mu=0.99, C_{\varepsilon1}=1.44, C_{\varepsilon2}=1.92, \sigma_k=1.0$, and $\sigma_\varepsilon=1.3$ [40,43]. After the velocity and pressure fields in the fluid domain were solved by the momentum equation, the k-ε model was used to obtain the turbulent kinetic energy and its dissipation rate. Then, the results of the k-ε model were incorporated into the momentum equation to account for the effect of turbulence and the flow characteristics were obtained.

2.1.2. Particle Motion Model

During IPP-Coring, the motion trajectories of the particles in the drilling fluid can be obtained by solving the motion equation in the Lagrangian domain, and the motion governing equation of the particles can result from Newton's second law [42,44]:

$$m_p\frac{d\left(\vec{v_p}\right)}{dt}=\vec{F_d}+\vec{F_g}+\vec{F_b}+\vec{F_p}+\vec{F_{vm}} \quad (7)$$

where m_p denotes the particle mass, $\vec{v_p}$ is the particle velocity, and $\vec{F_d}$, $\vec{F_g}$, $\vec{F_b}$, $\vec{F_p}$, and $\vec{F_{vm}}$ are the drag force, gravity force, buoyancy, pressure gradient force, and added mass force, respectively. Those forces can be expressed as [41,44]:

$$\vec{F_d}=\frac{3\mu C_D R_{e_r}}{4\rho_p {d_p}^2}m_p\left(\vec{u}-\vec{v_p}\right) \quad (8)$$

$$\vec{F_g} = m_p \vec{g} \tag{9}$$

$$\vec{F_b} = \frac{\pi {d_p}^3}{6}(\rho_p - \rho) \tag{10}$$

$$\vec{F_p} = \frac{\pi d_p^3 \rho}{6} \frac{Du}{Dt} \tag{11}$$

$$\vec{F_{vm}} = \frac{1}{12} \pi d_p^3 \rho_p \frac{d\vec{v_p}}{dt} \tag{12}$$

where C_D is the drag coefficient, R_{e_r} is the relative Reynolds numbers, ρ_p is the density of the particle, and d_p is the diameter of the particle [41].

2.1.3. Erosion Model

Due to the impingement of the particles in the drilling fluids on the surface of the differential motion assembly, erosion is inevitable. In this study, the E/CRC model was used to calculate the erosion rate, and the equations are as follows [45,46]:

$$E = CF_s(BH)^{-0.59} v^n F(\alpha) \tag{13}$$

$$F(\alpha) = 5.40\alpha - 10.11\alpha^2 + 10.93\alpha^3 - 6.33\alpha^4 + 1.42\alpha^5 \tag{14}$$

where E is the erosion rate, C is a coefficient of the erosion model, F_s is a coefficient of the particle shape, BH is the Brinell hardness of the material, v is the impact velocity of the particles, and α is the incidence angle of the particles colliding against the wall. In this study, the round sands were set as the erosion particles, and 42CrMo steel was the material used for the differential motion assembly. Therefore, $C = 15.59 \times 10^{-7}$, $F_s = 0.2$, $BH = 240$, and $n = 1.73$. After the impact velocity and angle of the particles were calculated by the above turbulence and particle motion model, the erosion rate can be quantified using Equations (13) and (14) in CFD.

2.2. Computational Domain

In this paper, the CFD module in COMSOL Multiphysics was used to conduct the CFD simulation of the flow channel of the differential motion assembly. According to the structure of the differential motion assembly, a 3D computational domain was built. Because of the symmetry of the fluid domain of the motion assembly and considering the cost of computational time, 1/4 of the fluid domain of the differential motion assembly was selected as the computational domain. Figure 2 shows the mesh and boundary conditions of the flow domain of the differential motion assembly. Hexahedral grids with high accuracy were built using sweep algorithms. The density of the drilling fluid was set as 1000 kg/m^3. To study the effect of the fluid viscosity, fluid viscosities of 1000, 100, 10, and 1 mPa·s were employed. The mass flow rate of the particles was set to 0.5 kg/s, and the density and the diameter of the sand particles were set as 2850 kg/m^3 and 6×10^{-5} m, respectively. According to the real working conditions of the differential motion assembly, the boundary conditions were set as follows:

Inlet: The boundary condition of the inlet was set as "fully developed flow", and flow rates of 0.01, 0.02, 0.03, and 0.04 m^3/s were set at the inlet to study the flow characteristics.

Wall: The inner surface of the differential motion assembly was set as the wall, no slip was selected for the wall, and the wall roughness parameter and the roughness height were set as 0.26 and 3.2 μm, respectively. In addition, the wall boundaries were set as "bounce" for the particles.

Outlet: The boundary condition of the outlet was set as the pressure condition, and according to the pump pressure in the field, the value of the pressure at the outlet was set as 30 MPa. In addition, the wall condition of the outlet for the particles was set as "Freeze".

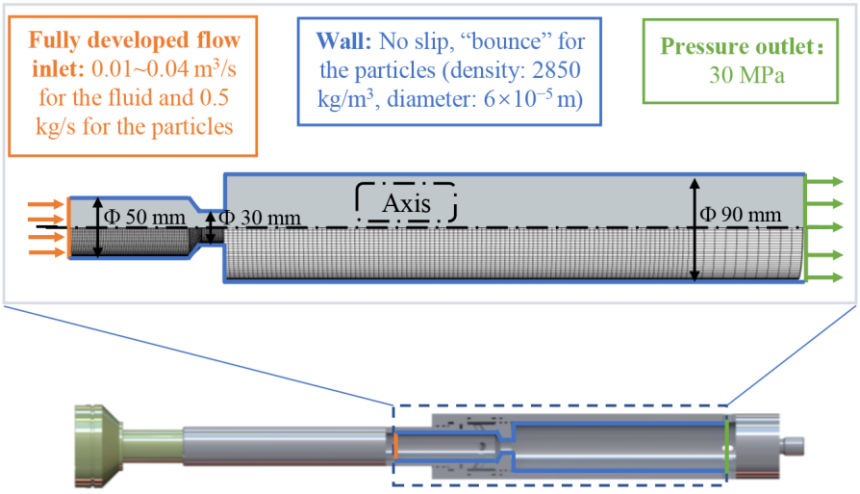


Figure 2. Mesh and boundary conditions of the flow domain in the differential motion assembly.

The velocity distributions along the radial direction at a line 150 mm away from the inlet under a flow rate of 0.04 m^3/s and fluid viscosity of 100 mPa·s were used to analyze the grid independency. The results of the grid independence study are shown in Figure 3; it shows that when the number of grids is more than 108,134, the solution is grid independent.

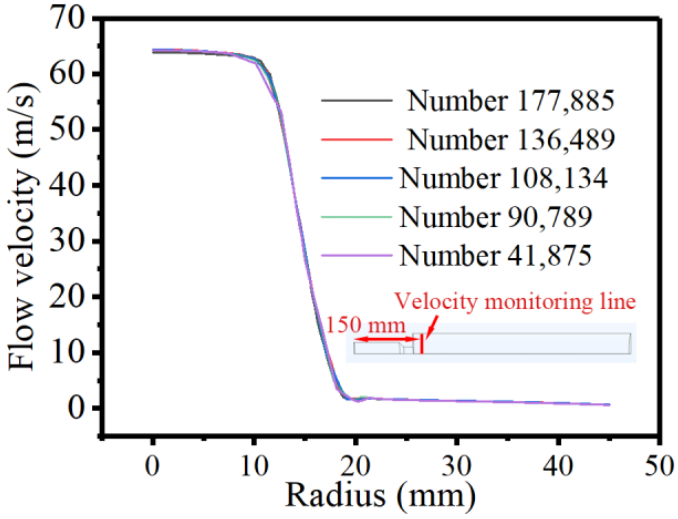


Figure 3. Grid independence study.

3. Results and Discussion

3.1. Flow Characteristics in the Differential Motion Assembly

The viscous effect is significant, and it is of great concern to the dynamic response of structures. Thus, in this study, the flow characteristics in the differential motion assembly with different fluid viscosities were studied first. The velocity streamlines in the differential motion assembly with different fluid viscosities are shown in Figure 4. It can be seen that a vortex area appeared in the differential motion assembly, and that the size of the vortex area increased as the viscosity of the fluid decreased from 1000 mPa·s to 1 mPa·s. To quantify the effect of the fluid viscosity on the flow velocity, we extracted the velocity at a monitoring line 220 mm away from the flow inlet, as shown in Figure 5. As seen in Figure 5, the maximum velocity in the monitoring line increased with the increase in the fluid viscosity, and the maximum in the monitoring line was 68 m/s for a fluid viscosity of 1000 mPa·s. These results demonstrate that increased fluid viscosity can increase the local velocity of the flow and decrease the size of the vortex area.

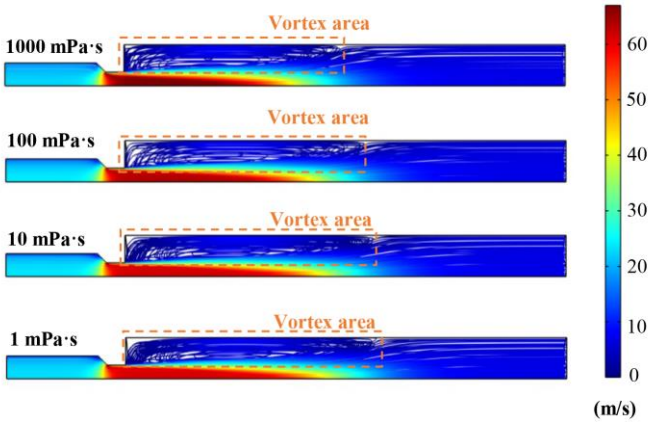


Figure 4. Velocity streamlines in the differential motion assembly with different fluid viscosities; the flow rate was 0.04 m^3/s.

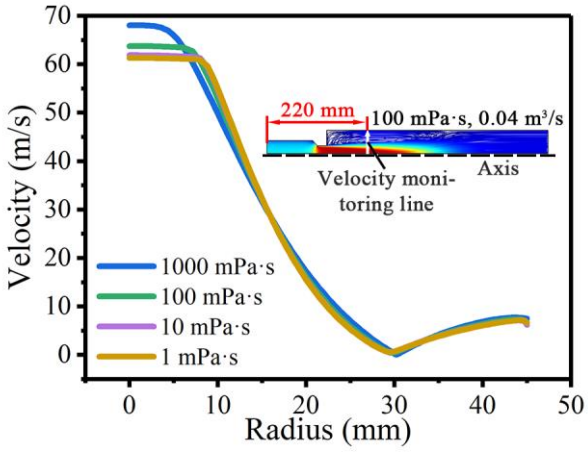


Figure 5. Velocity distributions at the monitoring line with different fluid viscosities; the flow rate was 0.04 m^3/s.

For the real working condition of the differential motion assembly, the fluid viscosity is usually about 100 mPa·s. Thus, we set the fluid viscosity as 100 mPa·s to study the effect of the flow rate and the inner structure. The flow characteristics of drilling fluid in the differential motion assembly, such as flow velocity and pressure distribution, directly affect the operational reliability and life of the assembly. Figure 6 shows the velocity streamlines in the differential motion assembly for different inlet flow rates. As the inlet flow rate increased, the velocity of the fluid in the differential motion assembly increased remarkably. The maximum velocity of 65 m/s appeared at the inlet of the ball seat for an inlet flow rate of 0.04 m^3/s. Although the diameter of the flow domain increased abruptly from 30 to 90 mm after the drilling fluid flowed through the ball seat, the drilling fluid near the axis still flowed a distance of about 200 mm at a relatively large velocity (e.g., at approximately 64 m/s when the inlet flow rate was 0.04 m^3/s) before the velocity of the fluid gradually decreased. However, due to the abrupt increase in the diameter of the flow domain at the outlet of the ball seat, a severe vortex was present near the wall of the differential motion assembly. The size of the vortex area showed almost no change for different inlet flow rates, which may be attributed to the same inner hydraulic structure. A vortex is a harmful flow characteristic that causes drilling fluid, which carries particles such as barite, to continuously impact and severely erode the inner wall of the differential motion assembly. Unfortunately, the inner wall with a diameter of 90 mm is a motion surface, and after the ball is dropped to trigger the differential motion assembly, this wall moves upward under hydrodynamic pressure to realize in situ pressure preservation. The erosion

of this wall causes sticking when the differential motion assembly moves upward and leads to the failure of the IPP-Coring system.

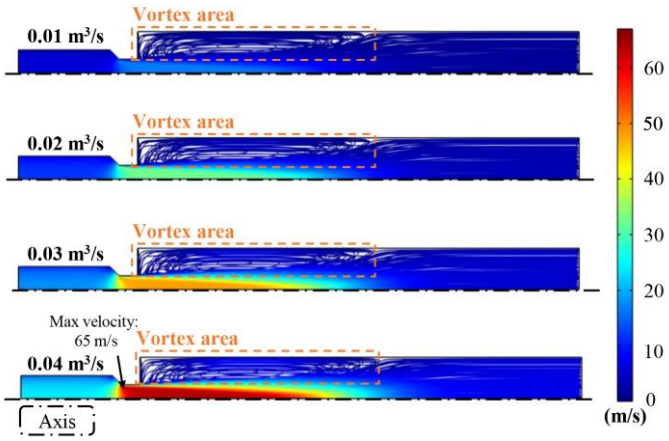


Figure 6. Velocity streamlines in the differential motion assembly with different inlet flow rates (0.01~0.04 m^3/s); the fluid viscosity was set as 100 mPa·s.

To further study the drilling fluid velocity distributions at the vortex area, we extracted the velocity at a monitoring line 220 mm away from the flow inlet, as shown in the inset illustration of Figure 7. The velocity distributions at the monitoring line with different inlet flow rates are shown in Figure 7. Along the radial direction, the flow area could be divided into the central jet area and vortex area according to the flow characteristics of the drilling fluid. In the central jet area, the velocity was stable at a larger value in the area with a radius less than 7 mm, such as 64 m/s for the inlet flow rate of 0.04 m^3/s. As the inlet flow rate decreased from 0.04 to 0.01 m^3/s, this velocity value gradually decreased to 16 m/s. With increasing radius, the velocity started to decrease and then gradually entered the vortex area where the velocity gradually decreased to nearly 0 m/s with increasing radius and then increased slowly. This trend conformed to the typical characteristics of the vortex. Near the wall with a diameter of 90 mm, the velocity of the vortex was relatively slow, less than 7.3 m/s. As the inlet flow rates decreased from 0.04 to 0.01 m^3/s, the velocity near the wall decreased from 7.3 to 1.9 m/s. At low velocity and small impact angles, the particles in the drilling fluid could still remove material from the wall with a diameter of 90 mm by plowing, which resulted in erosion [47]. As the flow rate increased from 0.01 to 0.04 m^3/s, although the size of the vortex area did not increase, the vortex velocity near the wall increased by 3.8-fold, which may lead to more severe surface erosion.

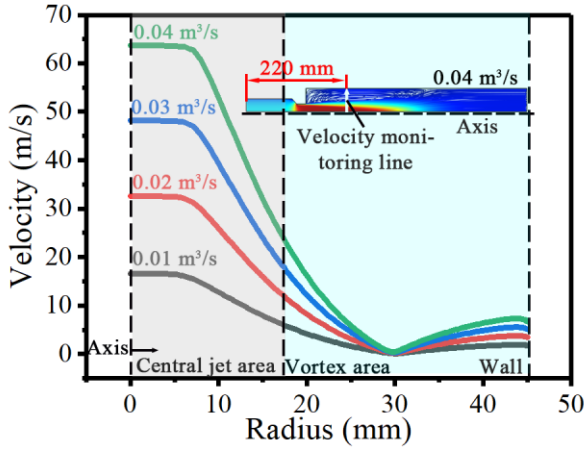


Figure 7. Velocity distributions at the monitoring line with different inlet flow rates; the fluid viscosity was set as 100 mPa·s.

Pressure contours in the differential motion assembly with different inlet flow rates are shown in Figure 8. There was an obvious pressure drop when the drilling fluid flowed through the differential motion assembly. In this study, the outlet pressure was set to 30 MPa during the calculation. With an increase in the inlet flow rate from 0.01 to 0.04 m^3/s, the inlet pressure increased from 30.1 to 31.4 MPa, and the pressure drop ΔP between the inlet and outlet of the differential motion assembly increased by 14-fold. Due to the greater pressure drop of 1.4 MPa when the inlet flow rate was 0.04 m^3/s, under the long-term impact of the drilling fluid, there is a risk of cutting the pins before the ball is dropped, which may trigger the differential motion assembly at the wrong time and result in the failure of the IPP-Coring process. Therefore, when a deep oil and gas IPP-Coring operation is conducted under large pump displacement, it is necessary to replace the pins with those of greater shear strength or diameter. In addition, the lowest pressure of 28.3 MPa (inlet flow rate 0.04 m^3/s) occurred at the inlet of the ball seat of the differential motion assembly where the flow velocity was extremely fast, up to 65 m/s. Therefore, severe erosion may occur in this zone due to the complex flow characteristics. In general, there was a severe vortex area in the differential motion assembly due to the presence of the ball seat and, with the increase in inlet flow rate, the velocity of the drilling fluid and the pressure drop between the inlet and outlet increased remarkably. These conditions may increase the erosion rate on the inner surface of the differential motion assembly and the risk of cutting the pin at the wrong time, which would damage the differential motion assembly and lead to the failure of the IPP-Coring process.

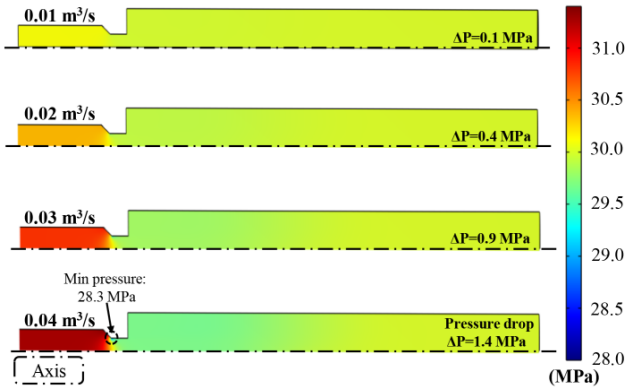


Figure 8. Pressure contours in the differential motion assembly with different inlet flow rates (0.01~0.04 m^3/s); the fluid viscosity was set as 100 mPa·s.

3.2. Effect of the Diameter of the Ball Seat on the Flow Characteristics

According to the analysis of the flow characteristics of the drilling fluid in the differential motion assembly, the flow had a higher velocity at the inlet of the ball seat, a severe vortex was present at the outlet of the ball seat near the wall, and the pressure drop reached 1.4 MPa when the inlet flow rate was 0.04 m^3/s. These characteristics will reduce the reliability and service life of the differential motion assembly. To improve these characteristics and further increase the success rate of IPP-Coring operations in deep oil and gas exploration, it is necessary to improve the local structure of the differential motion assembly.

Section 3.1 shows that the change in the flow status was largest at the ball seat. Therefore, we studied the effect of the diameter of the ball seat on the flow characteristics for ball seat diameters of 30, 35, and 40 mm. Figure 9 shows the effect of the diameter of the ball seat on the flow velocity. With the increase in the ball seat diameter, the velocity of the drilling fluid in the differential motion assembly decreased remarkably. The maximum velocity in the differential motion assembly with a 40 mm ball seat diameter decreased to 36 m/s, which was only 0.55 times that of the original assembly with a 30 mm ball seat diameter. In addition, the position of the maximum velocity changed; it was no longer at the inlet of the ball seat. This meant that the erosion at the inlet of the ball seat could be

improved more after the diameter of the ball seat was increased to 40 mm. In addition, in Figure 9, the axial length of the vortex area decreased to 0.85 times that of the original differential motion assembly with a 30 mm ball seat diameter when the ball seat diameter increased to 40 mm. To further study the velocity distributions in the vortex area, we extracted the velocity at the monitoring line for ball seats with different diameters, as shown in Figure 10. As the ball seat diameter increased from 30 to 40 mm, the velocity at the axis decreased from 64 to 35 m/s, and the velocity in the central jet area markedly decreased. Moreover, the distance of the vortex center (the place the velocity was near 0 m/s) with the axis increased from 29 to 33 mm. This meant that the radial length of the vortex area also decreased. Therefore, it can be concluded that the increase in the diameter of the ball seat decreased the size of the vortex area. Figure 10 also shows that when the diameter of the ball seat increased from 30 to 40 mm, the velocity near the wall in the vortex area decreased to 0.67 times that of the model with the original ball seat diameter. The decreases in the size of the vortex area and the vortex velocity near the wall would reduce erosion by drilling fluid and the risk of sticking when the differential motion assembly was triggered.

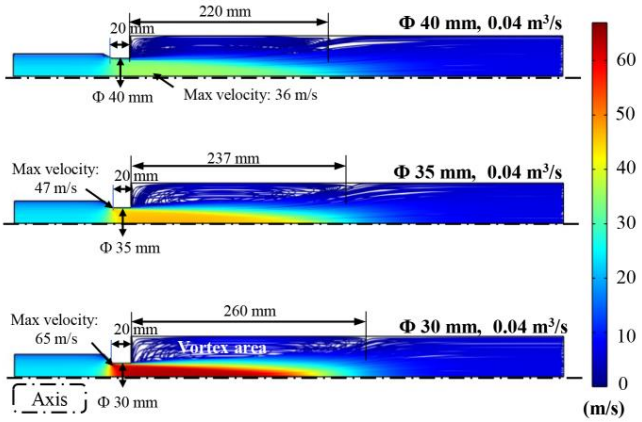


Figure 9. Effect of the diameter of the ball seat on the flow velocity; the fluid viscosity was set as 100 mPa·s.

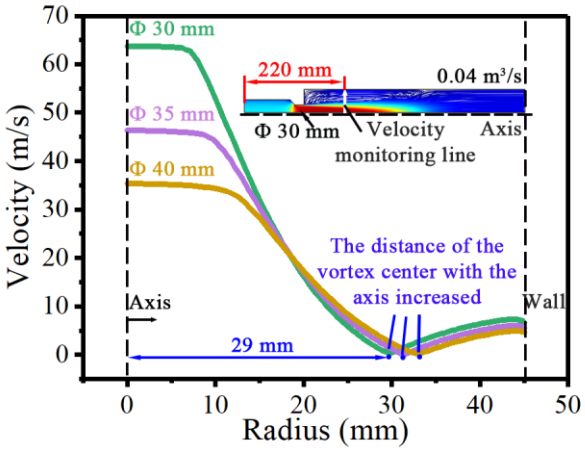


Figure 10. Velocity distributions at the monitoring line for ball seats with different diameters; the fluid viscosity was set as 100 mPa·s.

In addition to velocity changes, pressure changes also affect the service performance of the differential motion assembly. The larger pressure drop not only increases the load on the drilling pump and further results in unnecessary costs but can also increase the risk of cutting the pin before the ball is dropped, which would unexpectedly trigger the differential motion assembly and cause the IPP-Coring process to fail. Therefore, we studied the effect

of the diameter of the ball seat on the pressure distribution. As shown in Figure 11, as the diameter of the ball seat increased from 30 to 40 mm, the pressure at the inlet of the differential motion assembly decreased from 31.4 to 30.3 MPa, and the pressure drop ΔP of the differential motion assembly with a 40 mm ball seat diameter was only 0.2 times that of the assembly with a 30 mm ball seat diameter. In summary, when the ball seat diameter increased from 30 to 40 mm, the maximum velocity decreased to 0.55 times that of the original differential motion assembly with a ball seat diameter of 30 mm. The axial length of the vortex area and the vortex velocity near the wall decreased to 0.85 times and 0.67 times that for the original ball seat diameter, respectively. In addition, the pressure drop of the differential motion assembly with a ball seat diameter of 40 mm was only 0.2 times that of the original assembly. Thus, increasing the diameter of the ball seat could effectively reduce the erosion of the drilling fluid on the inner surface of the differential motion assembly and the risk of cutting the pin before the ball is dropped, thereby improving the reliability and service life of the differential motion assembly. Notably, the larger diameter of the ball seat in the differential motion assembly means that a larger drop ball should be used to trigger the differential motion assembly when a core enters the IPP-Coring system. However, due to the constraint of the inner diameter of the drilling tool, the diameter of the drop ball should not be too large; otherwise, it will be difficult to smoothly drop the ball onto the ball seat. As shown in Figure 2, the diameter of the inlet of the differential motion assembly was only 50 mm; therefore, a ball seat with a diameter of 40 mm may be the most appropriate.

3.3. Effect of the Outlet Structure of the Ball Seat on the Flow Characteristics

Increasing the diameter of the ball seat improved the flow status of the drilling fluid. However, due to the abrupt change of the diameter in the ball seat outlet, a severe vortex and turbulence occurred within the differential motion assembly. To reduce these behaviors, it is necessary to improve the outlet structure of the ball seat.

To study the effect of the outlet structure of the ball seat on the flow characteristics, and considering machining and structural strength factors, three outlet structures of the ball seat—arc, cone, and original right-angled structure—were designed, as shown in Figure 12. Their effect on the velocity is shown in Figure 13. The internal velocity distribution of the differential motion assembly of the cone outlet at the ball seat was similar to that of the original right-angled outlet. Their maximum velocities in the differential motion assembly were both 36 m/s at the axis behind the ball seat outlet. Notably, the arc ball seat outlet structure greatly decreased the fluid velocity in the differential motion assembly, and the maximum velocity was only 34 m/s at the ball seat inlet. In addition, the axial length of the vortex area in the differential motion assembly with a cone outlet structure at the ball seat was 211 mm, which was only 9 mm less than that for the original right-angled outlet. However, the axial vortex length in the differential motion assembly with the arc outlet structure decreased to 0.7 times that with the original right-angled outlet.

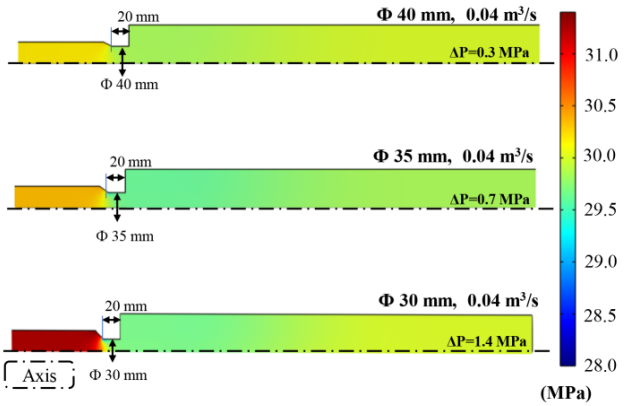


Figure 11. Effect of the ball seat diameter on the pressure distribution; the fluid viscosity was set as 100 mPa·s.

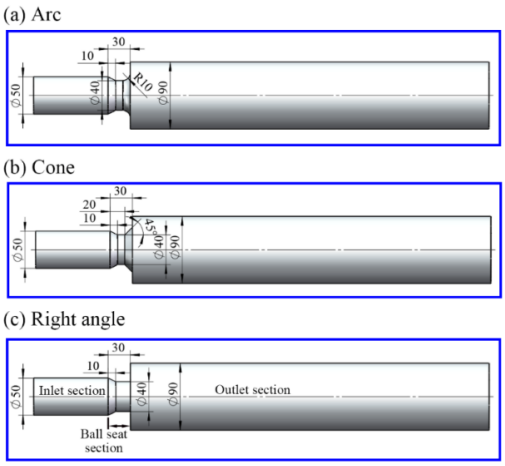


Figure 12. Differential motion assembly with different ball seat outlet structures: (**a**) arc, (**b**) cone, and (**c**) right angle.

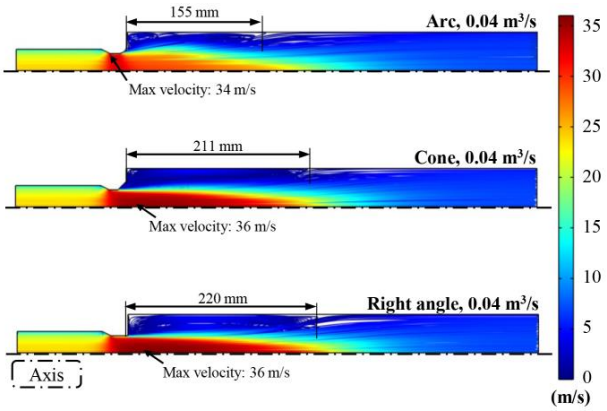


Figure 13. Effect of the outlet structure of the ball seat on the flow velocity; the fluid viscosity was set as 100 mPa·s.

To quantitatively study the effect of the outlet structure of the ball seat on the velocity distribution in the differential motion assembly, we set two velocity monitoring lines (shown in black and white) along the axial and radial directions, respectively. The velocity distributions at the two monitoring lines for different outlet structures at the ball seat are shown in Figure 14. In Figure 14a, according to the structural characteristics of the differential motion assembly, the computational domain of the differential motion assembly was divided into the inlet, ball seat, and outlet sections. The change in the outlet structure at the ball seat had almost no effect on the axial velocity distribution of the inlet section. However, when the drilling fluid entered the ball seat and outlet sections, the velocity of the arc structure was significantly less than that of the cone structure and the original right-angled structure. Notably, in the ball seat section of the arc structure, the drilling fluid first rose to 33 m/s and then started to decrease at the arc of the ball seat section. However, for the cone and original right-angled structure, the fluid continued to accelerate in the ball seat section. After entering the outlet section, the fluid continued to advance at a velocity greater than 35 m/s for approximately 130 mm before the velocity began to gradually decrease. In addition, as shown in Figure 14b, the maximum velocity of the central jet zone of the arc structure was only 28 m/s, which was 0.8 times that of the cone and the right-angled structure, and the vortex velocity near the wall of the arc structure was only 0.4 times that of the cone and right-angled structures. Therefore, it can be concluded that the arc structure in the ball seat outlet effectively decreased the fluid velocity in the differential motion assembly and improved the severe vortex and turbulence behaviors

in the differential motion assembly. Furthermore, the erosion of the inner surface of the differential motion assembly by the drilling fluid could be improved.

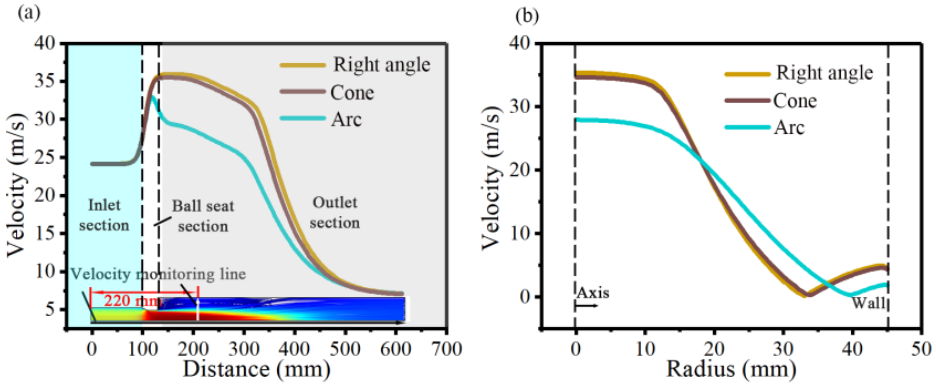


Figure 14. (**a**) Velocity distributions at the black velocity monitoring line with different diameters of the ball seat; (**b**) velocity distributions at the white velocity monitoring line with different diameters of the ball seat; the fluid viscosity was set as 100 mPa·s.

Figure 15 shows the effect of the outlet structure of the ball seat on the pressure distribution. There was a low-pressure zone in the ball seat section of the differential motion assembly with the arc ball seat outlet structure because the flow status changed at the arc. In addition, the pressure drops at the inlet and outlet of the differential motion assembly with the arc ball seat outlet structure were only 0.1 MPa, which was only 0.33 times that of the cone outlet and the right-angled outlet. In summary, the arc outlet ball seat not only greatly reduced the velocity of the drilling fluid and the severe vortex and turbulence behaviors in the differential motion assembly but also decreased the pressure drops in the differential motion assembly. Therefore, this outlet structure of the ball seat can reduce erosion by the drilling fluid and the risk of cutting the pin before the ball is dropped, which would improve the reliability and service life of the differential motion assembly as well as the success rate of the IPP-Coring procedure in deep oil and gas exploration.

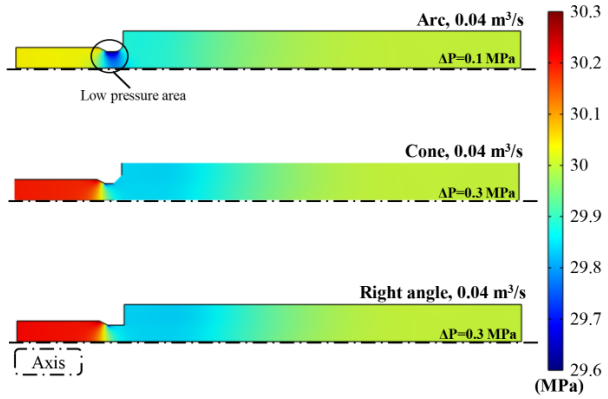


Figure 15. Effect of the outlet structure of the ball seat on the pressure distribution; the fluid viscosity was set as 100 mPa·s.

3.4. Structural Improvement of the Differential Motion Assembly of the IPP-Coring System

From the above results, the differential motion assembly with a 40 mm diameter ball seat and the arc structure in the ball seat outlet shows the lowest pressure drop and fluid velocity. To increase the operational reliability and service life of the differential motion assembly and further increase the success rate of IPP-Coring, this structure was chosen as the improved structure of the differential motion assembly. To quantitatively analyze the erosion of the improved structure, we further calculated the particle trajectories and the erosion of the original and improved differential motion assemblies when the fluid

viscosity was set as 100 mPa·s and the inlet flow rate was 0.04 m^3/s. As shown in Figure 16, compared with the original structure, the particles in the improved structure have a lower velocity and less impact on the wall. Therefore, the improved structure shows lower surface erosion, and the average erosion rate is only 0.42 times the value of the original structure. Due to the lower pressure drop and erosion rate, the improved structure has a smaller risk of sticking and triggering the assembly at the wrong time.

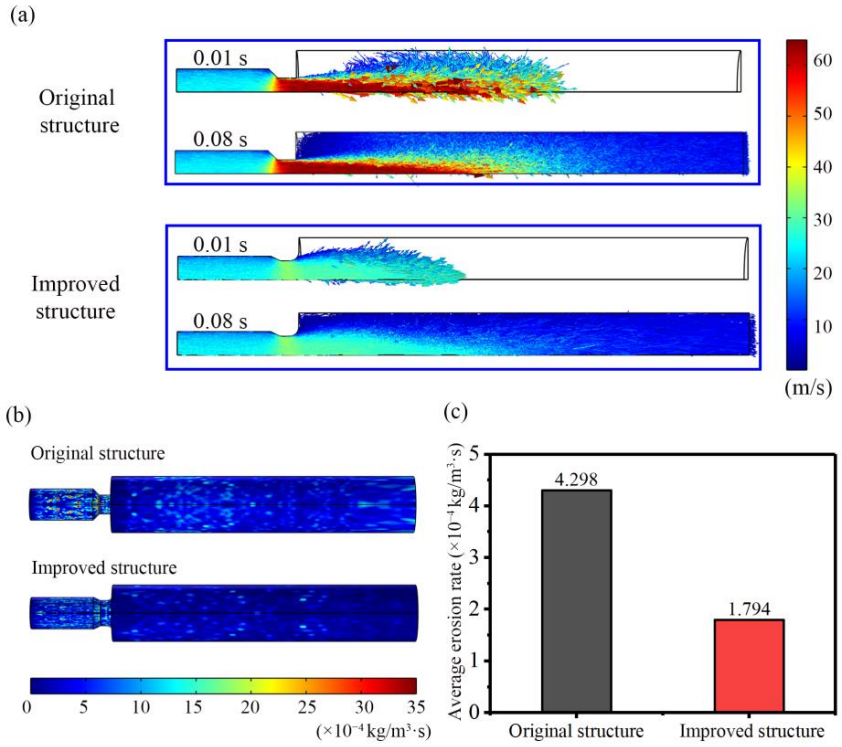


Figure 16. (**a**) Particle trajectories of the original and improved differential motion assembly; (**b**) the erosion contours of the original and improved differential motion assembly; (**c**) the average erosion rate of the original and improved differential motion assembly; the fluid viscosity was set as 100 mPa·s and the inlet flow rate was 0.04 m^3/s.

3.5. Field Validation Experiments

According to the CFD simulation results obtained above, the differential motion assembly was redesigned and manufactured. To validate the simulation results, field experiments were conducted in an experimental well in Tangshan, Hebei, China. During the experiments, the differential motion assembly with original and improved structure was installed in the IPP-Coring system, respectively, and then it was lowed into the well with a depth of 30 m. After that, the pump was turned on and the coring operation was conducted. The solid phase in the drilling fluid is mainly quartz sand and the field experimental conditions were summarized in Table 1.

Table 1. Field experimental conditions.

Parameter	Value
Flow rate (m^3/s)	0.01
Density of the drilling fluid (kg/m^3)	1050
Funnel viscosity of the drilling fluid (s)	60–70

The photographs of the outlet of the ball seat of the original and improved differential motion assemblies after the experiments are shown in Figure 17. It can be seen that there was obvious erosion damage at the outlet of the ball seat of the original differential motion

assembly, while the outlet of the ball seat of the improved differential motion assembly was relatively smooth and no obvious surface damage can be observed. In addition, the circulation pump pressure of the system with the improved differential motion assembly decreased from 0.2 MPa to nearly 0 MPa compared with that of the system with the original differential motion assembly. Therefore, it can be validated that the improved differential motion assembly shows the best erosion resistance and the lower pressure drop; thus, it has better promise for field performance.

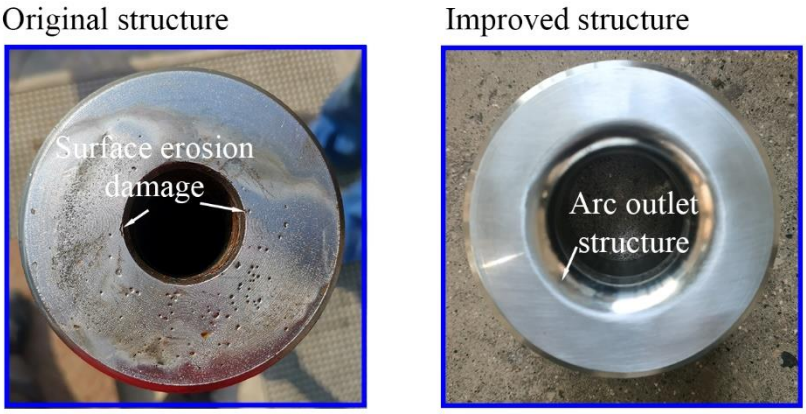


Figure 17. Photographs showing the outlet of the ball seat of the original and improved differential motion assemblies after the experiments.

4. Conclusions

In this study, CFD simulations were performed to investigate the flow characteristics in a differential motion assembly during the IPP-Coring process with different flow rates. The effects of the diameter of the ball seat and the structure of the ball seat outlet on the fluid status, velocity, and pressure distribution were thoroughly investigated. Thus, the hydraulic structure of the differential motion assembly was improved. The specific conclusions are presented as follows:

1. There was a severe vortex area in the differential motion assembly due to the presence of the ball seat. Increased fluid viscosity can increase the local velocity of the flow and decrease the size of the vortex area. In addition, as the inlet flow rate increased from 0.01 to 0.04 m^3/s, the vortex velocity near the wall and the pressure drops between the inlet and outlet of the differential motion assembly increased by 3.8- and 14-fold, respectively.
2. With the increase in the ball seat diameter from 30 to 40 mm, the maximum velocity in the differential motion assembly decreased to 0.55 times that of the original assembly. The axial length of the vortex area and the vortex velocity near the wall decreased to 0.85 and 0.67 times the values of the original assembly. In addition, the pressure drop decreased to 0.2 times that in the original assembly with a 30 mm ball seat diameter.
3. Compared with the cone and original right-angled structures, the arc structure at the ball seat outlet of the differential motion assembly showed the best hydraulic properties. Its axial vortex length and vortex velocity near the wall in the differential motion assembly decreased, respectively, to 0.7 and 0.4 times the values for the system with the original right-angled structure at the ball seat outlet. The pressure drop was only 0.33 times that of the system with the original right-angled structure at the ball seat outlet.
4. Considering the above results, the ball seat with a 40 mm diameter was selected for the differential motion assembly, and the outlet of the ball seat was set as the arc structure. The calculated results of the particle trajectories and the erosion show that the improved structure has lower particle velocity and less impact on the wall, and the average erosion rate decreased to 0.42 times the original structure. Due to the

lower pressure drop and erosion rate, the improved differential motion assembly may have better promise for field performance.

Author Contributions: Conceptualization, D.G. and J.L.; methodology, D.G., D.W. and Y.Z.; software D.G. and X.F.; validation, D.G., J.L. and D.W.; formal analysis, D.G. and X.F.; investigation, D.G. and Y.Z.; resources, H.X.; data curation, D.G.; writing—original draft preparation, D.G.; writing—review and editing, D.G., J.L. and H.X.; visualization, D.G.; supervision, H.X.; project administration, H.X.; funding acquisition, H.X. All authors have read and agreed to the published version of the manuscript.

Funding: The authors are grateful for the financial support from the National Natural Science Foundation of China (No. 51827901), the National Science Fund for Distinguished Young Scholars (No. 52225403) and the Sichuan Science and Technology Program (2023NSFSC0780).

Institutional Review Board Statement: Not applicable.

Informed Consent Statement: Not applicable.

Data Availability Statement: Raw or processed data required to reproduce these findings cannot be shared at this time, as the data also form part of an ongoing study.

Conflicts of Interest: The authors declare no conflict of interest.

References

1. Xie, H.P.; Zhu, J.B.; Zhou, T.; Zhang, K.; Zhou, C.T. Conceptualization and Preliminary Study of Engineering Disturbed Rock Dynamics. *Geomech. Geophys. Geo-Energy Geo-Resour.* **2020**, *6*, 34. [CrossRef]
2. Gao, M.Z.; Zhang, R.; Xie, J.; Peng, G.Y.; Yu, B.; Ranjith, P.G. Field Experiments on Fracture Evolution and Correlations between Connectivity and Abutment Pressure under Top Coal Caving Conditions. *Int. J. Rock Mech. Min. Sci.* **2018**, *111*, 84–93. [CrossRef]
3. Guo, D.; Xie, H.; Chen, L.; Zhou, Z.; Lu, H.; Dai, L. In-Situ Pressure-Preserved Coring for Deep Exploration: Insight into the Rotation Behavior of the Valve Cover of a Pressure Controller. *Pet. Sci.* 2023, *in press*. [CrossRef]
4. Xu, M.; Li, Y.; Chen, L.; Yang, X.; Duan, Z.; Fu, C.; Wang, D. Structural Design and Dynamic Simulation Optimization of the Triggering Device in a Pressure-Holding Controller for Deep In Situ Coring. *Appl. Sci.* **2022**, *12*, 4961. [CrossRef]
5. Xie, H.P.; Gao, F.; Ju, Y. Research and Development of Rock Mechanics in Deep Grounp Engineering. *Chin. J. Rock Mech. Eng.* **2015**, *34*, 2161–2678. [CrossRef]
6. Xie, H.P.; Gao, F.; Ju, Y.; Gao, M.Z.; Zhang, R.; Gao, Y.N.; Liu, J.F.; Xie, L.Z. Quantitative Definition and Investigation of Deep Mining. *J. China Coal Soc.* **2015**, *40*, 1–10. [CrossRef]
7. Xie, H.P.; Zhou, H.W.; Xue, D.J.; Wang, H.W.; Zhang, R.; Gao, F. Research and Consideration on Deep Coal Mining and Critical Mining Depth. *J. China Coal Soc.* **2012**, *37*, 535–542. [CrossRef]
8. Ashena, R.; Thonhauser, G. *Coring Methods and Systems*; Springer: Berlin/Heidelberg, Germany, 2018; ISBN 9783319777337.
9. Li, C.; Pei, J.L.; Wu, N.H.; Liu, G.K.; Huang, W.; Dai, Z.X.; Wang, R.Z.; Chen, Z.F.; Long, W.C. Rotational Failure Analysis of Spherical-Cylindrical Shell Pressure Controllers Related to Gas Hydrate Drilling Investigations. *Pet. Sci.* **2022**, *19*, 789–799. [CrossRef]
10. Xie, H.P.; Liu, T.; Gao, M.Z.; Chen, L.; Zhou, H.W.; Ju, Y.; Gao, F.; Peng, X.B.; Li, X.J.; Peng, R.D.; et al. Research on In-Situ Condition Preserved Coring and Testing Systems. *Pet. Sci.* **2021**, *18*, 1840–1859. [CrossRef]
11. Li, J.N.; Wang, J.; Hu, Y.Q.; You, Z.X.; Xu, M.; Wang, Y.W.; Zou, Z.J.; Kang, Q.Y. Contact Performance Analysis of Pressure Controller's Sealing Interface in Deep in-Situ Pressure-Preserved Coring System. *Pet. Sci.* **2022**, *19*, 1334–1346. [CrossRef]
12. He, Z.Q.; Yang, Y.; Yu, B.; Yang, J.P.; Jiang, X.B.; Tian, B.; Wang, M.; Li, X.Y.; Sun, S.Q.; Sun, H. Research on Properties of Hollow Glass Microspheres/Epoxy Resin Composites Applied in Deep Rock in-Situ Temperature-Preserved Coring. *Pet. Sci.* **2022**, *19*, 720–730. [CrossRef]
13. Hu, Y.Q.; Xie, J.; Xue, S.N.; Xu, M.; Fu, C.H.; He, H.L.; Liu, Z.Q.; Ma, S.M.; Sun, S.Q.; Wang, C.L. Research and Application of Thermal Insulation Effect of Natural Gas Hydrate Freezing Corer Based on the Wireline-Coring Principle. *Pet. Sci.* **2022**, *19*, 1291–1304. [CrossRef]
14. Bjorum, M. A New Coring Technology to Quantify Hydrocarbon Content and Saturation. In Proceedings of the Society of Petroleum Engineers-SPE Canadian Unconventional Resources Conference 2013-Unconventional Becoming Conventional: Lessons Learned and New Innovations, Calgary, AB, Canada, 5–7 November 2013; Volume 2, pp. 1159–1162. [CrossRef]
15. Hyland, C.R. Pressure Coring-an Oilfield Tool. In Proceedings of the Proceedings-SPE Annual Technical Conference and Exhibition, San Francisco, CA, USA, 5–8 October 1983. [CrossRef]
16. Zhu, H.; Liu, Q.; Deng, J.; Wang, G.; Xiao, X.; Jiang, Z.; Zhang, D. Pressure and Temperature Preservation Techniques for Gas-Hydrate-Bearing Sediments Sampling. *Energy* **2011**, *36*, 4542–4551. [CrossRef]
17. Liu, G.K.; Gao, M.Z.; Yang, Z.W.; Chen, L.; Fu, M.Q.; Xie, H.P. The Innovative Design of Deep in Situ Pressure Retained Coring Based on Magnetic Field Trigger Controller. *Adv. Civ. Eng.* **2020**, *2020*, 8873628. [CrossRef]
18. Merey, Ş. Drilling of Gas Hydrate Reservoirs. *J. Nat. Gas Sci. Eng.* **2016**, *35*, 1167–1179. [CrossRef]

19. Sun, Y.; Wang, Y.; Lü, X.; Jia, R.; Guo, W. Hole-Bottom Freezing Method for Gas Hydrate Sampling. *J. Nat. Gas Sci. Eng.* **2015**, *25*, 271–283. [CrossRef]
20. Li, C.; Xie, H.P.; Gao, M.Z.; Chen, L.; Zhao, L.; Li, C.B.; Wu, N.; He, Z.; Li, J. Novel Designs of Pressure Controllers to Enhance the Upper Pressure Limit for Gas-Hydrate-Bearing Sediment Sampling. *Energy* **2021**, *227*, 120405. [CrossRef]
21. He, Z.Q.; Chen, L.; Lu, T.; Xie, J. The Optimization of Pressure Controller for Deep Earth Drilling. *Therm. Sci.* **2019**, *23*, S877–S885. [CrossRef]
22. Chen, J.W.; Fan, W.; Bingham, B.; Chen, Y.; Gu, L.Y.; Li, S.L. A Long Gravity-Piston Corer Developed for Seafloor Gas Hydrate Coring Utilizing an in Situ Pressure-Retained Method. *Energies* **2013**, *6*, 3353–3372. [CrossRef]
23. Abid, K.; Spagnoli, G.; Teodoriu, C.; Falcone, G. Review of Pressure Coring Systems for Offshore Gas Hydrates Research. *Underw. Technol.* **2015**, *33*, 19–30. [CrossRef]
24. Kvenvolden, K.A.; Barnard, L.A.; Cameron, D.H. Pressure Core Barrel: Application to the Study of Gas Hydrates, Deep Sea Drilling Project Site 533, Leg 76. *Initial. Rep. DSDP* **1983**, *76*, 367–375. [CrossRef]
25. Milkov, A.V.; Dickens, G.R.; Claypool, G.E.; Lee, Y.J.; Borowski, W.S.; Torres, M.E.; Xu, W.; Tomaru, H.; Tréhu, A.M.; Schultheiss, P. Co-Existence of Gas Hydrate, Free Gas, and Brine within the Regional Gas Hydrate Stability Zone at Hydrate Ridge (Oregon Margin): Evidence from Prolonged Degassing of a Pressurized Core. *Earth Planet. Sci. Lett.* **2004**, *222*, 829–843. [CrossRef]
26. Dickens, G.R.; Paull, C.K.; Wallace, P. Direct Measurement of in Situ Methane Quantities in a Large Gas-Hydrate Reservoir. *Nature* **1997**, *385*, 426–428. [CrossRef]
27. Dickens, G.R.; Schroeder, D.; Hinrichs, K.-U. *The Pressure Core Sampler (PCS) on ODP Leg 201: General Operations and Gas Release. Texas: Ocean Drilling Program*; Texas A&M University: College Station, TX, USA, 2003; pp. 1–22.
28. Schultheiss, P.; Holland, M.; Humphrey, G. Wireline Coring and Analysis under Pressure: Recent Use and Future Developments of the HYACINTH System. *Sci. Drill.* **2009**, *7*, 44–50. [CrossRef]
29. Amann, H.; Hohnberg, H.J.; Reinelt, R. HYACE—A Novel Autoclave Coring Equipment for Systematic Offshore Gas Hydrate Sampling. *Dtsch. Wiss. Ges. Erdgas Kohle E.V.* **1997**, *9706*, 37–49.
30. Wakishima, R.; Imazato, M.; Nara, M.; Aumann, J.T.; Hyland, C. The Development of a Pressure Temperature Core Sample (PTCS) for the Recovery of in-Situ Methane Hydrates. In Proceedings of the International Symposium on Methane Hydrates; JNOC-TRC: Chiba, Japan, 1998; p. 107.
31. Yang, L.W.; Sun, W.T.; Luo, J.; Wang, G.Y.; Wang, J.M. Study and Application of GWY194-70BB Heat and Pressure Preservation Coring Tool. *OIL Drill. Prod. Technol.* **2014**, *36*, 58–61.
32. Yang, L.W.; Su, Y.; Luo, J.; Sun, S.L. Development and Application of GW-CP194-80A Pressure-Maintaining Coring Tool. *Nat. Gas Ind.* **2020**, *40*, 91–96.
33. Messa, G.V.; Yang, Q.; Adedeji, O.E.; Chára, Z.; Duarte, C.A.R.; Matoušek, V.; Rasteiro, M.G.; Sean Sanders, R.; Silva, R.C.; Souza, F.J. De Computational Fluid Dynamics Modelling of Liquid–Solid Slurry Flows in Pipelines: State-of-the-Art and Future Perspectives. *Processes* **2021**, *9*, 1566. [CrossRef]
34. Wang, Q.; Huang, Q.; Wang, N.; Wen, Y.; Ba, X.; Sun, X.; Zhang, J.; Karimi, S.; Shirazi, S.A. An Experimental and Numerical Study of Slurry Erosion Behavior in a Horizontal Elbow and Elbows in Series. *Eng. Fail. Anal.* **2021**, *130*, 105779. [CrossRef]
35. Quan, J.; Liu, X.; Wang, C.; Gu, Y.; Wang, C.; Jin, H. A Study on Corrosion Failure of the Circulation Line with Valve Openings in Atmospheric Tower Based on CFD. *Eng. Fail. Anal.* **2022**, *141*, 106633. [CrossRef]
36. Tang, Y.; Zhao, P.; Li, X.; Fang, X.; Yang, P. Numerical Simulation and Experimental Test of the Sliding Core Dynamics of a Pressure Controlled Jet Crushing Tool for Natural Gas Hydrate Exploitation. *Processes* **2022**, *10*, 1033. [CrossRef]
37. Tang, Y.; Jing, X.; Li, W.; He, Y.; Yao, J. Analysis of Influence of Different Convex Structures on Cooling Effect of Rectangular Water Channel of Motorized Spindle. *Appl. Therm. Eng.* **2021**, *198*, 117478. [CrossRef]
38. Alghurabi, A.; Mohyaldinn, M.; Jufar, S.; Younis, O.; Abduljabbar, A.; Azuwan, M. CFD Numerical Simulation of Standalone Sand Screen Erosion Due to Gas-Sand Flow. *J. Nat. Gas Sci. Eng.* **2021**, *85*, 103706. [CrossRef]
39. Zhao, J.; Zhang, G.; Xu, Y.; Wang, R.; Zhou, W.; Yang, D. Experimental and Theoretical Evaluation of Solid Particle Erosion in an Internal Flow Passage within a Drilling Bit. *J. Pet. Sci. Eng.* **2018**, *160*, 582–596. [CrossRef]
40. Zheng, C.; Liu, Y.; Wang, H.; Zhu, H.; Liu, Z.; Ji, R.; Shen, Y. Structural Optimization of Downhole Fracturing Tool Using Turbulent Flow CFD Simulation. *J. Pet. Sci. Eng.* **2015**, *133*, 218–225. [CrossRef]
41. Feng, C.; Liu, W.; Gao, D. CFD Simulation and Optimization of Slurry Erosion of PDC Bits. *Powder Technol.* **2022**, *408*, 117658. [CrossRef]
42. Yang, S.; Fan, J.; Zhang, L.; Sun, B. Performance Prediction of Erosion in Elbows for Slurry Flow under High Internal Pressure. *Tribol. Int.* **2021**, *157*, 106879. [CrossRef]
43. Pei, J.; Lui, A.; Zhang, Q.; Xiong, T.; Jiang, P.; Wei, W. Numerical Investigation of the Maximum Erosion Zone in Elbows for Liquid-Particle Flow. *Powder Technol.* **2018**, *333*, 47–59. [CrossRef]
44. Zheng, C.; Liu, Y.; Wang, H.; Zhu, H.; Liu, Z.; Cai, B.; Shen, Y. Numerical Study on Improving the Erosion Life of Ball Seat for Oil and Gas Reservoir Fracturing. *Eng. Fail. Anal.* **2016**, *60*, 188–198. [CrossRef]
45. Ahlert, K.R. Effects of Particle Impingement Angle and Surface Wetting on Solid Particle Erosion of AISI 1018 Steel. Ph.D. Thesis, University of Tulsa, Tulsa, OK, USA, 1994.

46. Zhang, Y.; Reuterfors, E.P.; McLaury, B.S.; Shirazi, S.A.; Rybicki, E.F. Comparison of Computed and Measured Particle Velocities and Erosion in Water and Air Flows. *Wear* **2007**, *263*, 330–338. [CrossRef]
47. Javaheri, V.; Porter, D.; Kuokkala, V.T. Slurry Erosion of Steel-Review of Tests, Mechanisms and Materials. *Wear* **2018**, *408–409*, 248–273. [CrossRef]

Disclaimer/Publisher's Note: The statements, opinions and data contained in all publications are solely those of the individual author(s) and contributor(s) and not of MDPI and/or the editor(s). MDPI and/or the editor(s) disclaim responsibility for any injury to people or property resulting from any ideas, methods, instructions or products referred to in the content.